Quantitative theoretical analysis of the electrostatic force between a metallic tip and semiconductor surface in Kelvin probe force microscopy

Nobuyuki Ishida

National Institute for Materials Science, 1-2-1 Sengen, Tsukuba, Ibaraki 305-0047, Japan

E-mail: ishida.nobuyuki@nims.go.jp

Takaaki Mano

National Institute for Materials Science, 1-2-1 Sengen, Tsukuba, Ibaraki 305-0047, Japan

October 2023

Abstract. Theoretical analysis of the electrostatic force between a metallic tip and semiconductor surface in Kelvin probe force microscopy (KPFM) measurements has been challenging due to the complexity introduced by tip-induced band bending (TIBB). In this study, we present a method for numerically computing the electrostatic forces in a fully three-dimensional (3D) configuration. Our calculations on a system composed of a metallic tip and GaAs(110) surface revealed deviations from parabolic behavior in the bias dependence of the electrostatic force, which is consistent with previously reported experimental results. In addition, we show that the tip radii estimated from curve fitting of the theory to experimental data provide reasonable values, consistent with the shapes of tip apex observed using scanning electron microscopy. The 3D simulation, which accounted for the influence of TIBB, enables a detailed analysis of the physics involved in KPFM measurements of semiconductor samples, thereby contributing to the development of more accurate measurement and analytical methods.

1. Background

Kelvin probe force microscopy (KPFM), a derivative of atomic force microscopy (AFM), is a pivotal analytical technique for measuring electrostatic potential distribution at the nanoscale [1–3]. Since its invention, KPFM has been widely used in characterizing various electronic [4–10] and ionic devices [11–16]. This method measures the contact potential difference (CPD) by detecting the bias voltage at which the electrostatic force between the probe tip and sample is minimized. The electrostatic force (F_{elec}) is generally explained using a parallel-plate capacitor model, where the force is proportional to the square of the bias voltage (U), displaying parabolic behavior in $F_{\mathrm{elec}}(U)$ characteristics. This behavior arises from the fact that for metal samples, the tip-sample capacitance is solely determined by the geometric positioning of the tip and sample, irrespective of the bias voltage. Consequently, the bias voltage of minimal electrostatic force can be determined by fitting a parabolic curve to the $F_{\mathrm{elec}}(U)$ characteristics [17–19].

However, the situation differs for semiconductor samples. In this case, the lines of electric force (or electric field) generated between the tip and the sample by the applied bias penetrate the semiconductor surface and enter the interior of the semiconductor, a phenomenon known as tip-induced band bending (TIBB) [20, 21]. The TIBB induces a change in the tip-sample capacitance depending on the bias voltage, leading to a deviation from the parabolic behavior in the $F_{\mathrm{elec}}(U)$ characteristics [10, 22]. The magnitude and length scales of the TIBB generally depend not only on the bias voltage but also on other parameters, including the tip radius, tip-sample separation, and doping density of the sample [21, 23]. The complex nature of the TIBB complicates theoretical analysis of the electrostatic force. Although several studies have theoretically examined the bias dependence of the electrostatic force for semiconductor samples, they have been limited to one-dimensional approximations [24–26]. In addition, a direct quantitative comparison between $F_{\mathrm{elec}}(U)$ spectra from experiments and theoretical calculations, a type of line-shape analysis, has yet to be conducted.

In this study, we developed a method for numerically computing the electrostatic force between a metallic tip and semiconductor surface in a fully three-dimensional (3D) model while considering the effect of the TIBB. To achieve this, we utilized the Poisson solver (SEMITIP) developed by Feenstra [21, 23, 27–30], which allowed us to calculate the electrostatic potential distribution in both the vacuum and semiconductor regions, induced by an applied potential from a metallic probe tip near the semiconductor surface. The electrostatic forces acting on the tip were calculated using the electric field and charge density on the tip surface as derived from the potential distribution provided by the SEMITIP. Due to the bias-dependent change in the magnitude of the TIBB, our calculation of the electrostatic force on a GaAs(110) surface revealed non-parabolic behavior in the $F_{\mathrm{elec}}(U)$ curve, which was consistent with our previously reported results [10]. We also achieved good quantitative agreement between the simulated spectra and the experiments. In addition, we demonstrated that the tip radii used in the experiments

can be estimated from the curve fittings. Direct comparisons of numerical computations and experiments enable a detailed analysis and rigorous understanding of the physics involved in KPFM measurements of semiconductor samples. Given that many of the samples analyzed by KPFM are semiconductors, our method provides significant benefits for achieving more precise electrostatic potential measurements and for advancing the development of new measurement and analytical methods.

2. Methods

2.1. Computation of electrostatic force using SEMITIP

The SEMITIP was originally developed to analyze experimental data obtained from scanning tunneling microscopy (STM) and spectroscopy (STS) [21, 23]. It can compute the electrostatic potential and resulting tunneling current produced by a metallic probe tip near the semiconductor surface. We extended the application range of the SEMITIP by developing a method to calculate the electrostatic forces acting between the tip and sample in AFM/KPFM measurements.

The electrostatic force per unit area ($\boldsymbol{f}_{\mathrm{elec}}$) acting on the surface of a conductor can be derived from the relationship $\boldsymbol{f}_{\mathrm{elec}} = \frac{1}{2}\sigma\boldsymbol{E}$, where σ is the surface charge density and $\boldsymbol{E}$ is the electric field on the conductor surface [31]. On a conductor surface, the electric field is always directed perpendicular to the surface and the magnitude can be computed as $E = \boldsymbol{E} \cdot \hat{\boldsymbol{n}} = -dV/dn$, where $\hat{\boldsymbol{n}}$ is the unit vector outward normal to the surface, V represents the electrostatic potential, and dV/dn is the rate of change in the surface-normal direction. In addition, the charge density on the conductor surface can be calculated using the relationship $\sigma = \varepsilon_0 E$, where ε_0 is the vacuum dielectric constant.

Based on these relationships, we calculate the electrostatic force acting on the tip surface using the electrostatic potential distribution near the tip surface. We used SEMITIP Ver.4, where calculations were performed using a cylindrical symmetric system [23, 32]. The radial direction is represented by r and the direction along the cylindrical axis is represented by z. The script in the "semitip_v4.f" file was slightly modified to output the coordinates (r and z values) of the grid points in the vacuum region and the electrostatic potential at each grid point. The details of the script modifications are presented in Supplementary Fig. S1.

In the SEMITIP, the electrostatic potential ($V_{i,j}$) in the vacuum regions was calculated using modified prolate spherical coordinates, denoted by ξ_i ($i = 1, 2, \ldots, m$) and η_j ($j = 1, 2, \ldots, n$). $V_{i,n}$ ($i = 1, 2, \ldots, m$) corresponds to the electrostatic potential at the tip surface. To calculate the electrostatic force, we first calculated the electric field on the tip surface along the η direction (E_i^{eta}) (η direction is the direction traveled when i is fixed and j is changed) as follows:

$$E_i^{\mathrm{eta}} = \frac{V_{i,n-1} - V_i}{\Delta l}, \tag{1}$$

where Δl is the distance between (ξ_i, η_{n-1}) and (ξ_i, η_n). The η direction was not always perpendicular to the tip surface. Thus, to obtain an electric field perpendicular to the

tip surface ($E = \boldsymbol{E} \cdot \hat{\boldsymbol{n}}$), E_i^{eta} was multiplied by $1/\cos\theta_i$, where θ_i is the angle between the surface normal and the lines connecting the two grid points (ξ_i, η_{n-1}) and (ξ_i, η_n). Subsequently, the surface charge density (σ) on the tip surface was calculated using the relationship: $\sigma = \varepsilon_0 E$. Finally, the electrostatic force per unit area ($\boldsymbol{f}_{\mathrm{elec}}$) acting on the tip surface was calculated based on the relationship $\boldsymbol{f}_{\mathrm{elec}} = \frac{1}{2}\sigma\boldsymbol{E}$.

2.2. SPM measurements

All the measurements were performed at 78 K under ultrahigh vacuum (UHV) conditions ($< 1 \times 10^{-8}$ Pa) using a low-temperature scanning probe microscopy (SPM) system (Unisoku USM-1400). The qPlus sensors with electrochemically etched tungsten (W) tips (P-100WS, Unisoku) were used as scanning probes. The resonance frequency of the sensor ranged from 24 to 31 kHz. The surface oxide layers on the W tips were removed by Ar^+-ion sputtering (1.5 kV) for 15 min. The forces acting between the tip and sample were acquired in frequency modulation (FM) mode [33] with an oscillation amplitude of 580 pm. The tip-sample separation was regulated using the STM mode, i.e, an averaged tunneling current was employed as the feedback signal. A bias voltage was applied to the sample with respect to the tip. The sample grown on an n-type GaAs(001) wafer with an n-type GaAs layer on top [10, 34] was cut into pieces of sizes of approximately 8 mm $\times$ 3 mm. The sample was cleaved at room temperature to obtain a clean GaAs(110) surface and was immediately transferred to the low-temperature SPM head.

3. Results and Discussion

3.1. Electrostatic force distribution on tip surface

Using the method described in Section 2.1, we computed the electrostatic force on a system composed of a metallic tip and n-type GaAs(110) surface (the doping density was set to 5×10^{17} cm^{-3}). The main input parameters of the SEMITIP are the bias voltage (U), tip radius (R_{tip}), tip-sample separation (s), and CPD. We used parameter values of -2.0 V, 15 nm, 1.53 nm, and -0.850 V for U, R_{tip}, s, and CPD, respectively, which are typical values assumed in actual experiments. The other parameter values are shown in Supplementary Table I. Note that the definition of CPD in the SEMITIP differs slightly from ours; thus, the actual input for CPD had the opposite sign (+0.850 V). In addition, we included the surface states originating from the Ga dangling bonds within the conduction band with a Gaussian-type energy distribution [29]. The spatial density was set to 4.4×10^{14} cm^{-2}, which corresponds to the spatial density of the Ga dangling bond. The energy position of the Gaussian distribution E_{SS} (defined as the energy difference between the centroid of the Gaussian distribution and the valence band maximum) and the full width at half maximum (FWHM) ΔE_{SS} were introduced as input parameters. E_{SS} and ΔE_{SS} were set to 1.936 eV and 0.25 eV, respectively.

Figure 1 shows the z component of the electrostatic force per unit area ($f_{\mathrm{elec}}^z = \boldsymbol{f}_{\mathrm{elec}} \cdot \hat{\boldsymbol{z}}$), presented as absolute values and plotted against the radial distance. Note

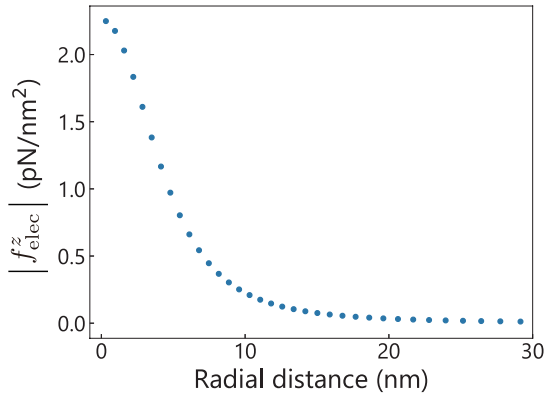

Figure 1. z component of the electrostatic force per unit area (f^z_{elec}) acting on the tip surface plotted as a function of the radial distance. The forces are expressed as absolute values.

that, in general, in AFM/KPFM measurements, only the z component of the atomic force is detectable. For clarity, the displayed range of r on the tip surface extended from 0 to 30 nm, although the computation covered a total range of approximately 2000 nm on the tip surface. A plot for the full range of r is presented in Supplementary Fig. S2. The distribution of the electrostatic force revealed a peak at the center of the tip apex, steeply diminishing along the radial direction and asymptotically approaching zero. At a distance of the tip radius, the force was reduced by approximately 94%. This result demonstrated that the electrostatic forces acting on the tip surface were predominantly concentrated within an area approximately equivalent to the tip radius.

The z component of the total electrostatic force (F^z_{elec}) acting on the tip can be computed by integrating $f^z_{\mathrm{elec}}dS$ along the radial direction, where dS is the area element, expressed as $2\pi r dr$. In this study, the direction of the force was configured such that a negative electrostatic force represented an attractive force. F^z_{elec} calculated using the data in Fig. 1 was -550 pN, which is consistent with the range of electrostatic forces typically observed experimentally [35].

3.2. Bias dependence of electrostatic force

Before discussing the bias dependence of the total electrostatic force acting on the tip, we explain the method for converting the calculated electrostatic force into the frequency shift measured in the actual experiments. In this study, we focused on KPFM measurements based on the FM mode of AFM [33]. In FM-AFM, the atomic forces between the tip and sample (F_{ts}) are indirectly measured through the shift in the resonance frequency of the oscillator $\Delta\nu$ (here, we use ν to express the frequency because the letter f is used for force). $\Delta\nu$ is approximately proportional to the force gradient $\mathrm{d}F_{\mathrm{ts}}/\mathrm{d}z$ when the oscillation amplitude of the tip is small [36, 37]. By contrast, for a large oscillation amplitude in which the force gradient shows a substantial distance

dependence during the oscillation cycle, it is expressed by [36, 37]:

$$\Delta\nu = -\frac{\nu_0}{kA^2}\langle F_{\mathrm{ts}} q(t)\rangle \tag{2}$$

where ν_0 is the resonance frequency of the oscillator, A is the oscillation amplitude of the tip, and k is the spring constant of the oscillator. $q(t)$ represents the deflection of the tip during the oscillation cycle, given by $q(t) = A\cos(2\pi\nu_0 t)$, where t is the time. The brackets represent the average over one oscillation cycle.

To obtain the term given in the brackets, we computed the total electrostatic forces (F^z_{elec}) at 10 tip positions in a single oscillation cycle. For the terms preceding the brackets, that is, $-\frac{\nu_0}{kA^2}$, the resonance frequency and oscillation amplitude were set to 25.813 kHz and 580 pm, respectively, based on the values used in the experiments. We used a k value of 1852 N/m, theoretically estimated from the dimensions of the oscillator (the qPlus sensor) used in the experiments.

The bias dependence of $\Delta\nu$, computed as described above, is depicted by the solid circles in Fig. 2, revealing a parabolic-like behavior. The bias dependence of F^z_{elec} (before conversion to $\Delta\nu$) is presented in Supplementary Fig. S3, showing a curve shape similar to that of $\Delta\nu$ signals. The blue dashed line in Fig. 2 represents the fitting of a quadratic function (2nd-order polynomial) to the simulated $\Delta\nu$ signals. The fitting curve failed to follow the curvature of the simulation, indicating deviations from the parabolic behavior of the $\Delta\nu(U)$ characteristics. This non-parabolic behavior can be attributed to the bias-dependent changes in the magnitude and length of the TIBB, leading to bias-dependent alterations in the tip-sample capacitance. The bias dependence of magnitude of the TIBB (ϕ_{surf}) measured relative to the potential energy at a point far inside the semiconductor is shown in Supplementary Fig. S4.

Due to the fitting errors, the CPD value obtained from the fitting (−0.657 V) deviated by approximately 0.2 V from the input CPD value (−0.850 V). By contrast, increasing the polynomial order for fitting significantly reduced the fitting errors, as illustrated by the orange dashed line in Fig. 2. Consequently, the CPD value derived from the fitting (−0.852 V) closely matched the input CPD value. These results were consistent with our previously reported findings [10]. However, assigning physical significance to an increase in polynomial order can be challenging. The success of the fitting is primarily attributed to the mathematical property whereby higher-order polynomials can follow the curvature of arbitrary curve shapes more accurately.

3.2.1. Effect of Fermi level pinning The aforementioned calculations were performed on a GaAs(110) surface. The GaAs(110) surface is distinctive because no surface states exist within the bandgap, and this results in a flat band from the bulk to the surface without Fermi-level pinning [38]. Because of this characteristic, the magnitude of the TIBB varies significantly depending on the bias voltage, as shown in Supplementary Fig. S4. However, in many samples observed with KPFM, Fermi-level pinning occurs because of surface states within the bandgap induced by surface reconstruction, oxidation, contaminations, and so on. In these cases, the bias dependence of the TIBB

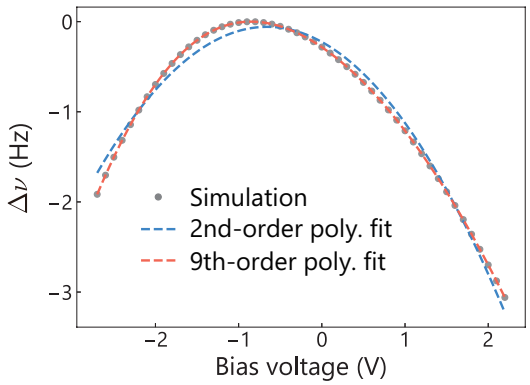

Figure 2. Bias dependence of $\Delta\nu$ signals computed using the GaAs(110) surface. Curve fittings of 2nd- and 9th-order polynomials to the simulated spectrum are represented by blue and orange dashed lines, respectively.

is expected to be highly suppressed. To incorporate the effect of Fermi-level pinning into our simulation, we introduced virtual surface states at the center of the bandgap of the GaAs(110) (0.756 eV above the top of the valence band), as depicted in Supplementary Fig. S5 and calculated electrostatic forces.

In Fig. 3(b), we show the $\Delta\nu(U)$ spectrum (solid circles) computed when considering the Fermi-level pinning effect. The blue dashed line represents the fitting curve using a 2nd-order polynomial, which closely follows the simulation without substantial deviation. This indicates that the simulated curve was nearly parabolic. This was because on this surface, the magnitude of the TIBB varied minimally with the bias voltage due to Fermi-level pinning, resulting in a nearly constant tip-sample capacitance. Consequently, the bias voltage at which the electrostatic force was minimized could be accurately determined by conventional parabolic curve fitting. However, the CPD value did not correspond to the difference in the work function between the tip (W_{tip}) and the sample (W_{sample}) but rather the value expressed as $((W_{\mathrm{sample}} + \phi^0_{\mathrm{surf}}) - W_{\mathrm{tip}})/e$ [25], where ϕ^0_{surf} is the magnitude of the intrinsic band bending of the surface (surface potential), and e is elementary charge. This result indicated that the CPD measured on a semiconductor surface was not necessarily the work function difference between the tip and sample but a value reflecting the surface potential.

3.2.2. Insight into standard KPFM measurement Till here, we have focused on the method known as Kelvin probe force spectroscopy (KPFS), where the $\Delta\nu(U)$ characteristic is obtained, and each curve is fitted with a polynomial function to determine the bias voltage at which the electrostatic force is minimized. However, there is another widely used method for KPFM, which involves applying bias modulation to either the tip or the sample and detecting the modulated force signals using a lock-in technique. In this method, the modulated force signal is minimized during KPFM measurements by adjusting the applied DC bias via a feedback circuit.

When the $\Delta\nu(U)$ characteristics deviate from the ideal parabolic behavior, the

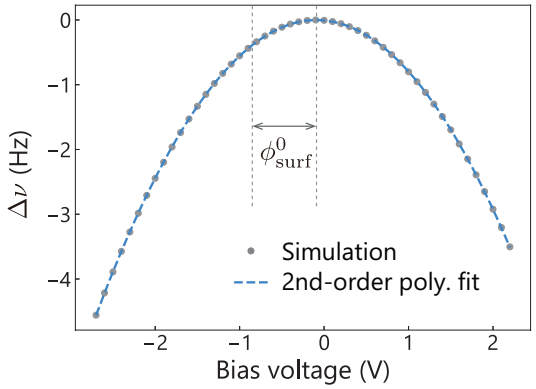

Figure 3. Bias dependence of $\Delta\nu$ signals computed using the GaAs(110) surface with virtual surface states at the center of the bandgap. Curve fittings of 2nd-order polynomials to the simulated spectrum are represented by blue dashed line. The positions of the input CPD value (−0.850 V) and the bias voltage corresponding to the minimal electrostatic force (−0.09 V) are indicated by vertical dashed lines.

modulation amplitude of the force signals detected by the lock-in technique does not respond linearly to the bias voltage. The lack of linearity may disturb accurate measurement of CPD [25] because the generally used feed back circuit assumes a linear response of the input signal.

One simple method to reduce the nonlinear effect is to minimize the amplitude of the modulation voltage as much as possible. However, this solution is often impractical, as an amplitude of approximately 1 V is typically required to ensure sufficient sensitivity for force detection. An alternative approach is to acquire $\Delta\nu(U)$ characteristics at several points on the sample before conducting the KPFM measurements and evaluate whether the curves deviate from parabolic behavior. If the $\Delta\nu(U)$ characteristics exhibit typical parabolic behavior, the CPD obtained through the feedback circuit can be assumed to be accurate. This scenario may occur when the surface band is strongly pinned, as explained in Section 3.2.1. On the other hand, if there is a deviation from parabolic behavior, switching to the KPFS method would be effective, although the measurement time would become significantly longer.

3.2.3. Tip radius dependence In Fig. 4, we show the simulated $\Delta\nu(U)$ spectra under tip radii of 5, 10, 30, 60, and 100 nm. The magnitude of the change in $\Delta\nu$ varies significantly depending on the tip radius. Similar situations are often encountered in actual experiments following accidental changes in the tip condition as a result of the tip crashing onto the surface. These changes are most likely induced by an increase in the tip radius resulting from a crash. Although the tip radius might appear to affect only the magnitude of the electrostatic force as a scaling factor, it also influences the curvature of the $\Delta\nu(U)$ spectrum across the entire bias range. This is because the tip radius affects the manner in which the TIBB changes depending on the bias voltage. In fact, a comparison of the normalized $\Delta\nu(U)$ spectra between tip radii of 5 and 100 nm

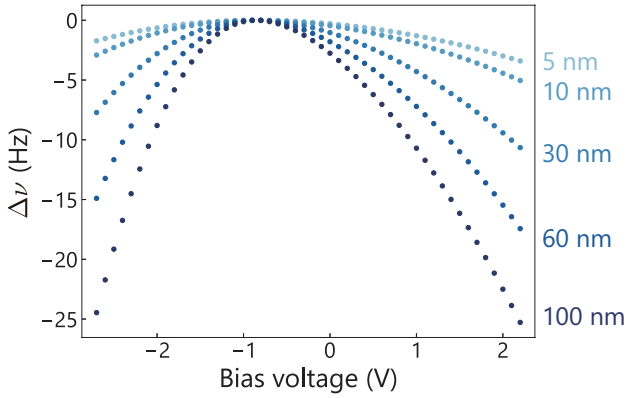

Figure 4. Simulated $\Delta\nu(U)$ spectra with varying tip radii of 5, 10, 30, 60, and 100 nm.

showed a discrepancy between the two curves, as depicted in Supplementary Fig. S6.

Next, we compare the simulated results with experimental data. For that, we estimated the radii of the W tips used in the experiments by fitting the simulated $\Delta\nu(U)$ spectra to the experimental data. The experimental spectra were obtained on the n-type GaAs(110) surfaces with a doping density of 5×10^{17} cm^{-3}. The tip-sample separations for the bias spectroscopy were regulated using the STM mode. The same set point (a bias voltage of -2.5 V and an averaged tunneling current of 50 pA) was used for all the experiments. The radius of each tip was also evaluated after the experiment by observing its apex with scanning electron microscopy (SEM) and fitting a hyperbolic curve, as used in the SEMITIP simulation, to the tip contour in the SEM image (see Supplementary Fig. S7). We performed the evaluations for nine W tips. According to the vendor, the typical tip radius of the as-provided W tips is less than 20 nm. To prepare W tips with larger radii, we heated the W tips with an electron beam (1 kV, 3-5 mA) in the UHV before attaching them to the qPlus sensors.

Figure 5 shows a typical result of the curve fitting after parameter optimization. The simulated curve showed good quantitative agreement with the experimental data, accurately reproducing the non-parabolic behavior of the $\Delta\nu(U)$ spectra. During the curve fittings, the CPD values were treated as fixed parameters, as they could be directly obtained from the experiments. The other main parameters were s and R_{tip}. Additionally, the term preceding the brackets in Eq. 2, $-\frac{\nu_0}{kA^2}$, was treated as a fitting parameter due to the uncertainty of k in the experiments. The uncertainty of s was expected to be less than 0.4 nm because the tip-sample separation was regulated using STM mode. To further narrow down the parameter range, we performed simultaneous fitting of simulated tunneling spectroscopy and force spectroscopy data to the experiment for one W tip, as explained in Supplementary Fig. S8. After that, the same value of s was used for fitting the simulations to the $\Delta\nu(U)$ spectra obtained with other W tips because the set point for the STM feedback was the same. While there still might be an uncertainty of ± 0.1 nm in s, within this small range, the change in the

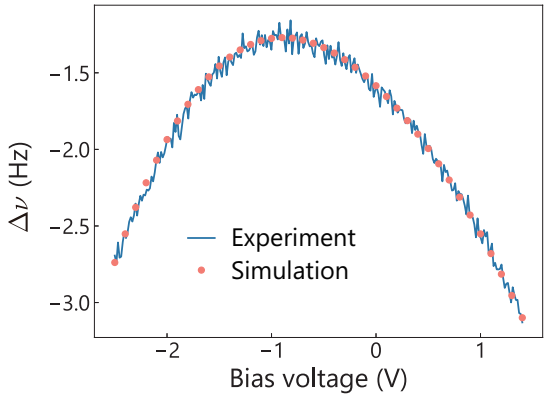

Figure 5. Experimentally obtained $\Delta\nu(U)$ curve on the GaAs(110) surface (solid line). The oscillation amplitude of the qPlus sensor was 580 pm. Solid circles show the simulated $\Delta\nu(U)$ curve using parameter values of 15 nm, 1.53 nm, and 0.892 V for R_{tip}, s, and CPD, respectively.

shape of the $\Delta\nu(U)$ spectra was small. The parameter that largely affected the shape of the $\Delta\nu(U)$ spectra was the value of R_{tip}. In our study, deviations from the optimal tip radius ($\pm$5 nm in R) prevented accurate fitting of the curvature on either side of the inflection point, as illustrated in Supplementary Fig. S9.

In Fig. 6, we plot the tip radii, with values estimated from the simulations on the horizontal axis and the values evaluated from SEM observations on the vertical axis. The tip radii evaluated from SEM observations approximately scaled with those estimated from the curve fittings. In most cases, the differences between the two evaluations were within $\pm$5 nm. These results suggest that fitting the simulated $\Delta\nu(U)$ spectra to the experimental data is effective for estimating the radius of the tip used in experiments. The tip radius can also be estimated from the simulation of the tunneling spectroscopy data using SEMITIP [18]. However, since the curve shape of $\Delta\nu(U)$ spectra is more sensitive than that of tunneling spectra, electrostatic force simulation can significantly narrow down the parameter range.

3.2.4. Tip-sample separation dependence We also investigated the tip-sample separation dependence of the simulated $\Delta\nu(U)$ spectra and compared them with the experiments. In the experiments, $\Delta\nu(U)$ spectra were obtained by lifting the tip from the tip-sample separation regulated by STM feedback (a bias voltage of -2.5 V and an averaged tunneling current of 50 pA). The lift heights were 0.0, 0.1, 0.3, 0.5, 1.0, and 3.0 nm. In the simulations, the experimental data with a lift height of 0.0 nm was first curve-fitted with the simulation by parameter optimization. Subsequently, we computed $\Delta\nu(U)$ spectra by only changing the tip-sample separation according to the lift heights. The tip radius estimated from the parameter optimization was 12 nm, which was within the typical range of radius for W tips used in our study.

The $\Delta\nu(U)$ spectra from the experiments and simulations are displayed in Fig. 7 as solid lines and solid circles, respectively. In the experiments, the atomic force between

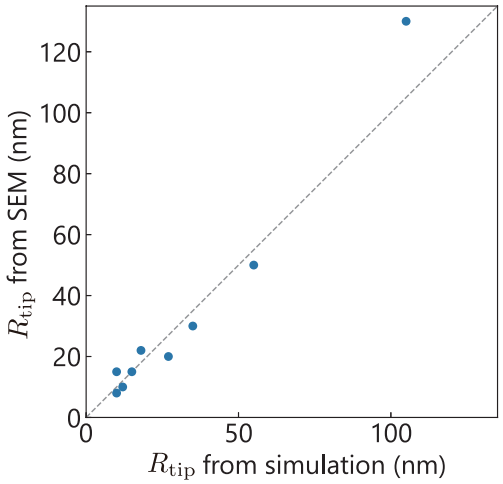

Figure 6. Plots of tip radii evaluated using two methods: curve fitting of theoretical models and SEM observations. The horizontal axis represents the tip radii estimated from the curve fittings, while the vertical axis shows the radii obtained from SEM observations.

the tip and sample (or $\Delta\nu$) did not reach zero, even at the bias voltage corresponding to the CPD due to the contribution from the van der Waals force. Therefore, we added offsets to the $\Delta\nu$ signals in the simulation for the comparisons.

For the data with a lift height of 0.0 nm, a fairly good agreement between theory and experiment was achieved after parameter optimization. Furthermore, the spectra simulated with increased tip-sample separations also quantitatively agreed well with the experimental values without further parameter optimization. These results show that the physical model used in the SEMITIP and the calculation of electrostatic force are plausible for reproducing the experiments. However, when a W tip having a larger tip radius (105 nm) was used, slight deviations were observed in fitting the simulated spectra to the experiments with increased tip heights, as displayed in Supplementary Fig. S10. These discrepancies could not be mitigated by changing several parameters including the tip-sample separation regulated by STM feedback and the tip radius. So far, we have not been able to clarify the reason behind the discrepancies. In the future, the model of SEMITIP may need to be improved to increase calculation accuracy for large tip radii.

4. Summary

We developed a method for calculating the electrostatic forces between a metallic tip and semiconductor surface, which has been challenging in previous studies due to the complexity introduced by the TIBB. We showed that our calculations were consistent with the expected properties of the electrostatic force, including (i) the concentration of the force around the tip apex, (ii) a parabolic-like behavior in the bias dependence, (iii) a minimum electrostatic force occurring at the bias voltage corresponding to the CPD, and

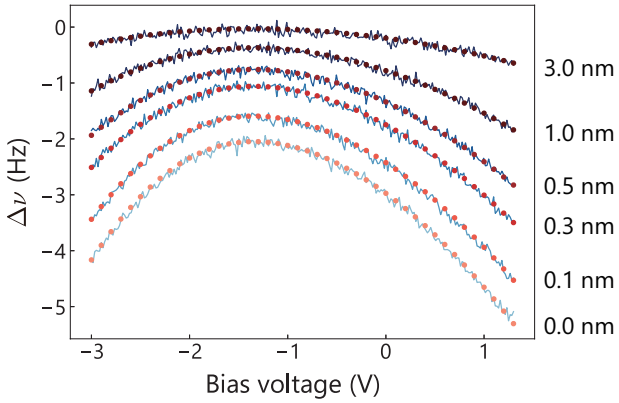

Figure 7. Tip-sample separation dependence of the $\Delta\nu(U)$ spectra from the experiments (solid lines) and simulations (solid circles). The offsets from the tip-sample separation regulated by the STM feedback were 0.0, 0.1, 0.3, 0.5, 1.0, and 3.0 nm.

(iv) a magnitude of the electrostatic force ranging from pN to nN. Simulations conducted on a GaAs(110) surface exhibited a $\Delta\nu(U)$ spectra that deviated from parabolic behavior due to a bias-dependent change in the TIBB, leading to a bias-dependent variation in the tip-sample capacitance. Curve fitting of the simulated $\Delta\nu(U)$ spectra to experimental data showed good quantitative agreement. In addition, we demonstrated that the tip radii used in the experiments could be estimated from the curve fitting with an accuracy of approximately 10 nm. The SEMITIP software used for the electrostatic force computation is capable of handling inhomogeneous samples, including p-n junctions and hetero-interfaces of semiconductors. Thus, our method can be used for future theoretical analysis of physics involved in the KPFM measurements, including the manner in which the tip radius and oscillation amplitude affect the spatial resolution of KPFM and the extent to which the strength of Fermi-level pinning affects CPD measurements.

Acknowledgments

We would like to thank R. M. Feenstra for the fruitful discussion concerning the calculation of the electrostatic force using the SEMITIP. This work was partially supported by JSPS KAKENHI Grant Numbers JP17K06366, JP21H01818, and JP24K01367.

References

References

[1] Nonnenmacher M, O'Boyle M P and Wickramasinghe H K 1991 *Appl. Phys. Lett.* **58** 2921

[2] Melitz W, Shen J, Kummel A C and Lee S 2011 *Surf. Sci. Rep.* **66** 1

[3] Sadewasser S and Glatzel T (eds) 2012 *Kelvin Probe Force Microscopy: Measuring and Compensating Electrostatic Forces* (Springer)

[4] Shikler R, Meoded T, Fried N and Rosenwaks Y 1999 *Appl. Phys. Lett.* **74** 2972

[5] Glatzel T, Sadewasser S, Shikler R, Rosenwaks Y and Lux-Steiner M C 2003 *Mater. Sci. Eng. B* **102** 138

[6] Cai M, Ishida N, Li X, Yang X, Noda T, Wu Y, Xie F, Naito H, Fujita D and Han L 2018 *Joule* **2** 296

[7] Noda T, Ishida N, Mano T and Fujita D 2020 *Appl. Phys. Lett.* **116** 163501

[8] Nakamura T, Ishida N, Sagisaka K and Koide Y 2020 *AIP Adv.* **10** 085010

[9] Hiraoka M, Ishida N, Matsushita A, Uchida R, Sekimoto T, Yamamoto T, Matsui T, Kaneko Y, Miyano K, Yanagida M and Shirai Y 2022 *ACS Appl. Ener. Mater.* **5** 4232

[10] Ishida N and Mano T 2023 *Nanotechnology* **35** 065708

[11] Luchkin S Y, Amanieu H Y, Rosato D and Kholkin A L 2014 *J. Power Sources* **268** 887

[12] Masuda H, Ishida N, Ogata Y, Ito D and Fujita D 2017 *Nanoscale* **9** 893

[13] Masuda H, Matsushita K, Ito D, Fujita D and Ishida N 2019 *Commun. Chem.* **2** 140

[14] Otoyama M, Yamaoka T, Ito H, Inagi Y, Sakuda A, Tatsumisago M and Hayashi A 2021 *J. Phys. Chem. C* **125** 2841

[15] Ishida N 2022 *Beilstein J. Nanotechnol.* **13** 1558

[16] Ishida N 2022 *J. Phys. Chem. C* **126** 17627

[17] Vančura T, Kičin S, Ihn T, Ensslin K, Bichler M and Wegscheider W 2003 *Appl. Phys. Lett.* **83** 2602

[18] Münnich G, Donarini A, Wenderoth M and Repp J 2013 *Phys. Rev. Lett.* **111** 216802

[19] Albrecht F, Fleischmann M, Scheer M, Gross L and Repp J 2015 *Phys. Rev. B* **92** 235443

[20] Feenstra R M and Stroscio J A 1987 *J. Vac. Sci. Technol. B* **5** 923

[21] Feenstra R M, Dong Y, Semtsiv M P and Masselink W T 2006 *Nanotechnology* **18** 044015

[22] Schwarz A, Allers W, Schwarz U D and Wiesendanger R 2000 *Phys. Rev. B* **62** 13617

[23] Feenstra R M 2003 *J. Vac. Sci. Technol. B* **21** 2080–2088

[24] Hudlet S, Saint Jean M, Roulet B, Berger J and Guthmann C 1995 *J. Appl. Phys.* **77** 3308

[25] Xu J and Chen D 2021 *J. Appl. Phys.* **129** 034301

[26] Fukuzawa R, Liang J, Shigekawa N and Takahashi T 2022 *Jpn. J. Appl. Phys.* **61** SL1005

[27] Feenstra R M, Gaan S, Meyer G and Rieder K H 2005 *Phys. Rev. B* **71** 125316

[28] Dong Y, Feenstra R M, Semtsiv M P and Masselink W T 2008 *J. Appl. Phys.* **103** 073704

[29] Ishida N, Sueoka K and Feenstra R M 2009 *Phys. Rev. B* **80** 075320

[30] Gaan S, He G, Feenstra R M, Walker J and Towe E 2010 *J. Appl. Phys.* **108** 114315

[31] Griffiths D J 2017 *Introduction to Electrodynamics* (Cambridge University Press)

[32] SEMITIP Version 4 `https://www.andrew.cmu.edu/user/feenstra/`

[33] Albrecht T R, Grütter P, Horne D and Rugar D 1991 *J. Appl. Phys.* **69** 668

[34] Ishida N, Mano T and Noda T 2022 *Appl. Surf. Sci.* **583** 152373

[35] Falter J, Langewisch G, Hölscher H, Fuchs H and Schirmeisen A 2013 *Phys. Rev. B* **87** 115412

[36] Giessibl F J 2001 *Appl. Phys. Lett.* **78** 123

[37] Giessibl F J 2003 *Rev. Mod. Phys.* **75** 949

[38] Mönch W 2001 *Semiconductor Surfaces and Interfaces, Third edition* (Springer)